PIER C

(Received 29 January 2026, Accepted 7 March 2026, Scheduled 28 April 2026)

Design of a Ku-Band HTS Narrowband Hairpin Filter Based on Quarter-Wavelength Microstrip Line

Panpan Zhang[1], Chenhao Xu[1], Yiqiuzi Shen[1], Chenchen Wang[2], and Li Ding[1,*]

[1]*School of Health Science and Engineering, University of Shanghai for Science and Technology, Shanghai 200093, China*
[2]*School of Optoelectronic Information and Computer Engineering, University of Shanghai for Science and Technology, Shanghai 200093, China*

ABSTRACT: Microstrip-line filters face two major challenges in high-frequency applications. On the one hand, as the operating frequency increases, the resonator length becomes significantly shorter, and when its dimensions become comparable to the line width, the fabrication tolerances deteriorate markedly. However, especially for narrowband filters, the insertion loss becomes more pronounced. To meet the performance requirements of high-frequency narrowband filters in the Ku band, this paper presents the design and implementation of a seventeenth-order hairpin-line bandpass filter utilizing high-temperature superconducting (HTS) materials. The proposed filter operated at a center frequency of 15 GHz with a fractional bandwidth of 2%. By employing a high-permittivity substrate and $YBa_2Cu_3O_7$ superconducting thin-film technology, a compact structure with dimensions of 27.68 mm×3.62 mm×0.5 mm is achieved. The experimental results demonstrate that at 77 K, the filter exhibits an in-band insertion loss below 0.35 dB, a return loss better than 19.5 dB, and stopband suppression exceeding 40 dB, indicating excellent frequency selectivity and out-of-band rejection performance. This work verifies the application potential of HTS materials in high-frequency planar narrowband filters and provides an effective solution for the design of high-performance RF front-ends in the Ku band.

1. INTRODUCTION

In modern radio frequency (RF) and microwave systems, filters are fundamental components for signal selection and out-of-band interference suppression, and their performance directly affects system sensitivity, interference immunity, and link stability. With the continuous expansion of communication and sensing technologies toward higher frequency bands, spectrum resources have become increasingly congested, and the electromagnetic environment has become more complex. Consequently, more stringent requirements are imposed on the front-end signal processing performance. Under such circumstances, narrowband filters capable of simultaneously achieving steep transition bands and deep stopband suppression within a limited passband have become effective tools for mitigating adjacent-channel interference and improving the spectral efficiency [1–4]. However, the design of high-frequency narrowband filters is severely constrained by the increased conductor losses, higher coupling accuracy requirements, and enhanced parasitic mode effects. As a result, trade-offs among low insertion loss, strong stopband suppression, structural miniaturization, and manufacturing feasibility have become increasingly pronounced. Therefore, diversified structural configurations and implementation approaches must be explored to satisfy the demanding requirements of high-frequency narrowband applications.

Currently, three main technological approaches are widely adopted for high-frequency narrowband filter implementations. The first approach involves three-dimensional metallic waveguide structures, such as rectangular and gap waveguides. Owing to their low conductor loss and intrinsically high unloaded quality factor (Q), these structures exhibit superior performance in achieving sharp roll-off characteristics and deep stopband rejection and have been extensively applied in the Ku band and beyond [5–7]. Nevertheless, their large volume, high weight, and stringent machining and assembly tolerances render them unsuitable for high-density planar integration. The second approach employs substrate integrated waveguide (SIW) structures and their derivatives, which effectively reduce the size and weight while maintaining relatively high Q factors and facilitating integration with planar circuits. Enhanced selectivity can be achieved using multimode cavities and cross-coupling techniques [8–10]. Despite these advantages, SIW-based designs still face a trade-off between increased insertion loss and enlarged physical dimensions when extremely narrow bandwidths are required [11–13]. The third approach relies on conventional planar microstrip structures, which benefit from mature fabrication processes and low costs. However, at high frequencies, the relatively low unloaded Q of microstrip resonators makes it difficult to simultaneously achieve a low insertion loss and strong stopband suppression in narrowband applications. Overall, existing research on high-frequency narrowband filters has predominantly focused on waveguide-based solutions, whereas planar implementations remain comparatively underexplored.

High-temperature superconducting (HTS) technology offers an effective pathway for overcoming the performance limi-

* Corresponding author: Li Ding (sunnylding@usst.edu.cn).

tations of planar filters in high-frequency narrowband applications. From a physical perspective, superconductivity is a macroscopic quantum phenomenon, and its microwave response directly reflects the quantum coherence of the cooper pairs. HTS thin films exhibit extremely low surface resistance at cryogenic temperatures, which significantly enhances the unloaded Q of resonators. Consequently, planar filters with performances approaching that of waveguide devices can be realized in terms of low insertion loss and strong out-of-band suppression [14–17]. This advantage enables HTS filters to demonstrate unique values in application scenarios that have extremely stringent performance requirements. For instance, in superconducting quantum computing systems, the qubit coherence times are highly sensitive to external electromagnetic interference. HTS filters have become essential components for protecting quantum systems and improving operational fidelity owing to their outstanding noise suppression capability in the microwave frequency range. In recent years, several studies have combined HTS materials with resonator configurations, such as spiral resonators [18] and multi-ring resonators [19], to successfully realize planar filters operating below the Ku band that simultaneously exhibit narrow bandwidth, high selectivity, and compact size, thereby validating the potential of this technology. Nevertheless, systematic investigations of Ku-band HTS planar narrowband filters remain limited.

In this study, a seventeenth-order narrowband, highly selective hairpin-line bandpass filter based on high-temperature superconducting materials is proposed and experimentally demonstrated. The filter operated at a center frequency of 15 GHz with a relative bandwidth of 2%. The measurements show an in-band insertion loss below 0.35 dB, a return loss better than 19.5 dB, and an out-of-band suppression exceeding 40 dB. The proposed design fully exploits the high-Q characteristics of HTS materials and the spatial compactness of the linearly cascaded resonator configuration. Without sacrificing planar circuit integrability, it successfully reconciles the core performance requirements of narrowband low insertion loss and deep out-of-band suppression, thereby providing a viable technical solution for realizing high-performance Ku-band planar filters.

2. PRINCIPLE OF THE HAIRPIN BANDPASS FILTER

Hairpin microstrip bandpass filters consist of multiple half-wavelength resonators. Each basic resonator was folded into a U-shaped structure from a microstrip line with an electrical length of approximately half the guided wavelength, thereby achieving the required electrical length within a limited substrate area. This folding configuration preserves the half wavelength resonance condition while enhancing the electromagnetic coupling between the folded arms, enabling filter miniaturization without compromising the narrowband and high-selectivity performance. Multiple hairpin resonators were arranged sequentially on the same dielectric substrate according to the designed coupling scheme. Energy transfer between adjacent resonators is realized through parallel-coupled microstrip sections with an electrical length of approximately one-quarter of the guided wavelength, forming an overall bandpass filter that satisfies the desired specifications.

The fundamental coupled microstrip section was first analyzed for electromagnetic modeling of a hairpin bandpass filter. This section can be represented as a symmetric coupled microstrip line with an electrical length θ. Under even-mode excitation, the characteristic impedance is denoted as Z_{0e}, whereas under odd-mode excitation, it is denoted as Z_{0o}, as illustrated in Fig. 1(a).

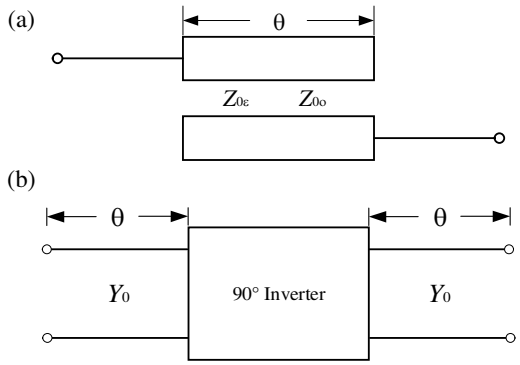

FIGURE 1. Coupled microstrip section and its equivalent circuit. (a) Coupled microstrip section. (b) Equivalent circuit of the J-inverter.

Based on transmission-line theory, the coupled structure is decomposed into even- and odd-mode components [20], yielding the corresponding impedance matrix shown in (1).

$$Z = \begin{bmatrix} -\frac{j}{2}\left(Z_{0e}+Z_{0o}\right)\cot\theta & -\frac{j}{2}\left(Z_{0e}-Z_{0o}\right)\frac{1}{\sin\theta} \\ -\frac{j}{2}\left(Z_{0e}-Z_{0o}\right)\frac{1}{\sin\theta} & -\frac{j}{2}\left(Z_{0e}+Z_{0o}\right)\cot\theta \end{bmatrix} \quad (1)$$

During the filter synthesis process, to establish a unified circuit representation between the coupled microstrip lines and the prototype network, the structure is commonly modeled as a two-port network and described using the transmission ABCD matrix. Compared with impedance or admittance parameters, the ABCD matrix is more suitable for characterizing properties of the cascaded network and is therefore widely employed in filter synthesis and analysis. For symmetric coupled microstrip lines, an equivalent model can be established using the even-odd mode decomposition method. By incorporating the even-mode impedance, odd-mode impedance, and electrical length, the corresponding equivalent transmission matrix A_1 can be derived, as given in (2).

$$A_1 = \begin{bmatrix} \frac{Z_{0e}+Z_{0o}}{Z_{0e}-Z_{0o}}\cos\theta & -\frac{j}{2}\cdot\frac{\left(Z_{0e}+Z_{0o}\right)^2\cos^2\theta-\left(Z_{0e}-Z_{0o}\right)^2}{\left(Z_{0e}-Z_{0o}\right)\sin\theta} \\ 2j\cdot\frac{\sin\theta}{Z_{0e}-Z_{0o}} & \frac{Z_{0e}+Z_{0o}}{Z_{0e}-Z_{0o}}\cos\theta \end{bmatrix} \quad (2)$$

To further establish a correspondence between the coupled microstrip line and the admittance inverter model in the low-pass prototype circuit, the coupled section is commonly represented by a cascaded structure consisting of a transmission line admittance inverter transmission line, as illustrated in Fig. 1(b). In this model, the two transmission lines have identical characteristic admittance Y and electrical length θ, while the intermediate inverter is characterized by the inverter constant J. Based on the cascade property of the transmission matrices, the overall transmission matrix of this equivalent structure, denoted as

TABLE 1. Normalized coupling matrix of the 17th-order filter.

$M_{1,2}$	$M_{2,3}$	$M_{3,4}$	$M_{4,5}$	$M_{5,6}$	$M_{6,7}$	$M_{7,8}$	$M_{8,9}$
0.0180	0.0121	0.0110	0.0106	0.0104	0.0103	0.0103	0.0102
$M_{9,10}$	$M_{10,11}$	$M_{11,12}$	$M_{12,13}$	$M_{13,14}$	$M_{14,15}$	$M_{15,16}$	$M_{16,17}$
0.0102	0.0103	0.0103	0.0104	0.0106	0.0110	0.0121	0.0180

A_2, can be derived as shown in (2). Under narrowband approximation, this modeling approach enables an approximate one-to-one correspondence between the distributed coupling characteristics and the lumped admittance inverter parameters, thereby providing a theoretical foundation for mapping prototype parameters to geometrical dimensions.

$$A_2 = \begin{bmatrix} \cos\theta & \frac{j}{Y_0}\sin\theta \\ jY_0\sin\theta & \cos\theta \end{bmatrix}\begin{bmatrix} 0 & -\frac{j}{J} \\ -jJ & 0 \end{bmatrix}\begin{bmatrix} \cos\theta & \frac{j}{Y_0}\sin\theta \\ jY_0\sin\theta & \cos\theta \end{bmatrix}$$
$$= \begin{bmatrix} \left(\frac{J}{Y_0}+\frac{Y_0}{J}\right)\cos\theta\sin\theta & j\left(\frac{J}{Y_0^2}\sin^2\theta - \frac{\cos^2\theta}{J}\right) \\ j\left(\frac{Y_0^2\sin^2\theta}{J} - J\cos^2\theta\right) & \left(\frac{J}{Y_0}+\frac{Y_0}{J}\right)\cos\theta\sin\theta \end{bmatrix} \quad (3)$$

By performing an element-by-element comparison, the ABCD matrix (A_1) derived from the coupled microstrip lines is further simplified, yielding closed-form expressions for the even- and odd-mode characteristic impedances in terms of the admittance inverter constant J

$$Z_{oe} = \frac{1}{Y_0}\left[1 + \frac{J}{Y_0} + \left(\frac{J}{Y_0}\right)^2\right] \quad (4)$$

$$Z_{oo} = \frac{1}{Y_0}\left[1 - \frac{J}{Y_0} + \left(\frac{J}{Y_0}\right)^2\right] \quad (5)$$

$$J_{01} = Y_0 \cdot \sqrt{\frac{\pi FBW}{2g_0g_1}} \quad (6)$$

$$J_{n,n+1} = Y_0 \cdot \sqrt{\frac{\pi FBW}{2g_Ng_{N+1}}} \quad (7)$$

$$J_{i,i+1} = Y_0 \cdot \frac{\pi FBW}{2\omega}\frac{1}{\sqrt{g_ig_{i+1}}}, \quad i = 1, 2, \ldots, N-1 \quad (8)$$

The above relationships explicitly establish a quantitative link between the admittance inverter parameter and the even- and odd-mode characteristic impedances of the coupled lines, thereby providing theoretical support for extracting the geometrical dimensions of the microstrip coupling structure from the circuit synthesis results. Furthermore, the inverter constant itself can be determined from the normalized parameters g_i of the low-pass prototype filter, fractional bandwidth FBW, characteristic admittance Y of the transmission line, and cutoff frequency of the low-pass prototype ω, as given by (6)–(8).

Equations (6)–(8) establish the correspondence between the normalized low-pass prototype parameters and admittance inverter constants, enabling the normalized design parameters obtained from the circuit synthesis to be directly mapped to the numerical values of the inverter model. In conjunction with the analytical relationships between the inverter constant and the even- and odd-mode characteristic impedances given in (4) and (5), respectively, a systematic mapping from the filter prototype parameters to the geometrical parameters of the distributed coupled-line structure can be achieved. This framework provides a solid foundation for parameter transformation between circuit-level design and physical implementation.

3. FILTER STRUCTURE DESIGN

In this design, a Chebyshev bandpass filter synthesis approach was adopted with a passband ripple of 0.01 dB. The center frequency was set to $f = 15$ GHz, the fractional bandwidth was $FBW = 2\%$, and the filter order was $N = 17$. The substrate was selected with a relative dielectric constant $\varepsilon = 9.8$ and a thickness of 0.5 mm to ensure stable electrical performance at high frequencies. Then, through calculation, the low-pass prototype g-values can be obtained. $g = g_{18} = 1.0000$, $g_1 = g_{17} = 1.0427$, $g_2 = g_{16} = 1.4883$, $g_3 = g_{15} = 2.0260$, $g_4 = g_{14} = 1.7193$, $g_5 = g_{13} = 2.1354$, $g_6 = g_{12} = 1.7614$, $g_7 = g_{11} = 2.1622$, $g_8 = g_{10} = 1.7729$, $g_9 = 2.1683$. During the design process, the synthesis is first carried out based on filter synthesis theory, starting from a normalized low-pass prototype filter to obtain the element parameters. A bandpass transformation was then applied to derive the admittance inverter parameters for each stage. On this basis, the resulting electrical parameters were further mapped to the geometrical dimensions of the structure by exploiting the even- and odd-mode characteristic impedance relationships of the hairpin resonators, thereby establishing the initial physical model of the filter. According to the method presented in [21], the coupling coefficients between adjacent resonators, $M_{i,i+1}$, and the external quality factors Q_{ei} and Q_{eo} can be derived from the low-pass prototype parameters, with the corresponding relationships given in (9) and (10).

$$M_{i,i+1} = \frac{FBW}{\sqrt{g_ig_{i+1}}} \quad (9)$$

$$Q_{ei} = \frac{g_0g_1}{FBW}, Q_{eo} = \frac{g_ng_{n+1}}{FBW} \quad (10)$$

The calculated results yielded external quality factors of $Q_{ei} = Q_{eo} = 41.71$. The normalized coupling coefficients between the adjacent resonators are listed in Table 1.

To investigate the coupling characteristics between the hairpin resonators, a simulation model consisting of two identical resonators was constructed, and parametric simulations were performed to analyze the influence of variations in the relative

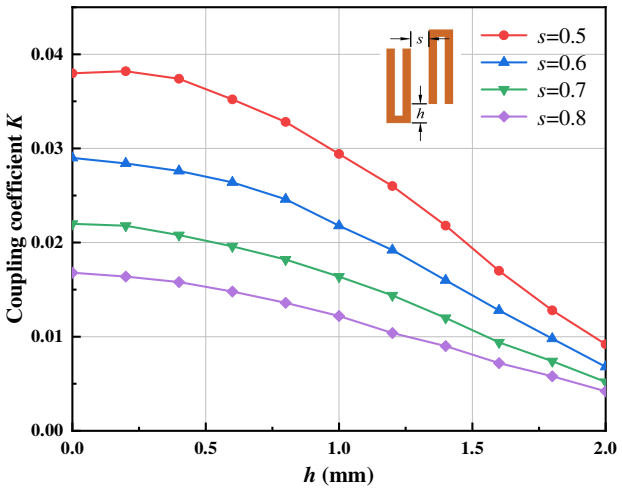

FIGURE 2. Variation of the coupling coefficient with relevant parameters.

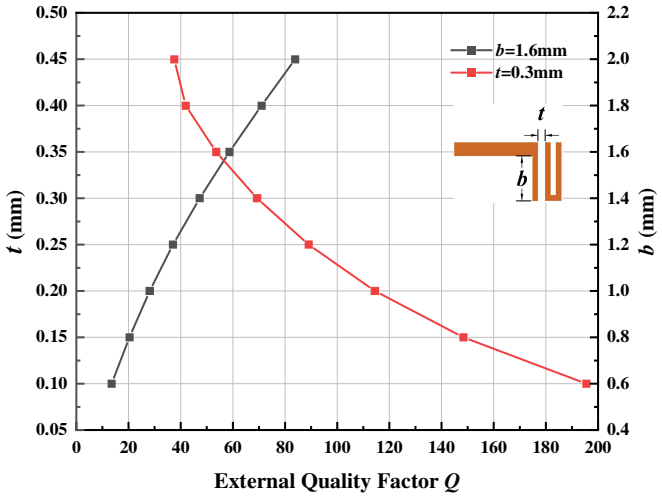

FIGURE 3. Variation of the external quality factor with coupling gap t and feed-line length b.

spacing between resonators on the coupling strength. The coupling strength between adjacent resonators is characterized by the coupling coefficient $K_{i,j}$, which can be calculated from the lower and higher resonant frequencies f_1 and f_2 of the coupled resonators [22], as expressed in (11).

$$K_{i,j} = \frac{f_2^2 - f_1^2}{f_2^2 + f_1^2} \tag{11}$$

During the simulation process, the resonator spacing s and parallel coupling height h between adjacent resonators were varied independently, and the corresponding lower and higher resonant frequencies are recorded to extract the coupling coefficients. The results indicate that when the parallel coupling height h is kept constant, reducing the spacing s enhances the electromagnetic coupling between the adjacent resonators, leading to an increase in the coupling coefficient. Conversely, for a fixed spacing s, increasing the parallel coupling height h weakened the electromagnetic interaction within the coupling region, resulting in a reduced coupling coefficient. Fig. 2 presents the coupling coefficient as a function of the coupling-related parameters, where different curves correspond to different coupling conditions, providing a clear illustration of the influence of these parameters on coupling strength.

To realize the energy coupling between the filter ports and the resonators and to effectively control the external quality factor, a tapped-line indirect coupling scheme was adopted in the design. The feed line is placed parallel to the coupling edge of the first and last resonators and separated from the resonators by a coupling gap t, through which energy transfer is achieved via electromagnetic field interaction. Under a single-resonator loaded model, the external quality factor is typically extracted using the 3 dB bandwidth method, with the corresponding expression given in (12).

$$Q_e = \frac{f_0}{\delta_{f_{3\,\mathrm{dB}}}} \tag{12}$$

Here, f denotes the resonant frequency of the resonator, and $\delta_{f_{3\,\mathrm{dB}}}$ represents the corresponding 3 dB bandwidth. Fig. 3 illustrates the simulated variation in the external quality factor Q_e as a function of the geometric parameters. It can be observed that with the feed-line length b kept constant, increasing the coupling gap t weakens the electromagnetic coupling between the port and the resonator, resulting in an increased Q_e Conversely, for a fixed coupling gap t, increasing the inserted feed line length b enhanced the coupling strength, thereby reducing Q_e. These results indicate that the desired external coupling strength can be flexibly achieved through the combined adjustment of coupling gap t and the feed line length b. According to the external quality factor Q_e theoretically calculated from (9), the coupling gap and feed-line length are finally determined to be $t = 0.27$ mm and $b = 1.6$ mm, respectively.

Based on the theoretically synthesized parameters, the filter was modeled and optimized using the full-wave electromagnetic simulation software IE3D. The resonator lengths, inter-resonator spacing, and tapped-line feeding positions were treated as optimization variables, whereas the passband insertion loss and out-of-band suppression were adopted as the primary optimization objectives. Through this process, a structural configuration that satisfied the design specifications was determined. The filter was implemented using a high-temperature superconducting thin film microstrip process. Considering fabrication feasibility, both the microstrip line widths and the coupling gaps are designed to be larger than 0.1 mm to ensure consistency between fabrication accuracy and electrical performance. The overall structure of the filter consisted of 17 linearly cascaded hairpin resonators arranged in a centrally symmetric layout. The detailed geometrical dimensions and layout of the proposed filter are illustrated in Fig. 4.

Figure 5(a) shows the simulated S-parameter responses of the filter. It can be observed that the filter exhibits a flat passband response around the center frequency of 15 GHz, with a minimum insertion loss better than 0.2 dB. The in-band return loss remained higher than 19.6 dB, accompanied by steep skirt characteristics at the passband edges. Moreover, a suppression level exceeding 40 dB is achieved over the stopband re-

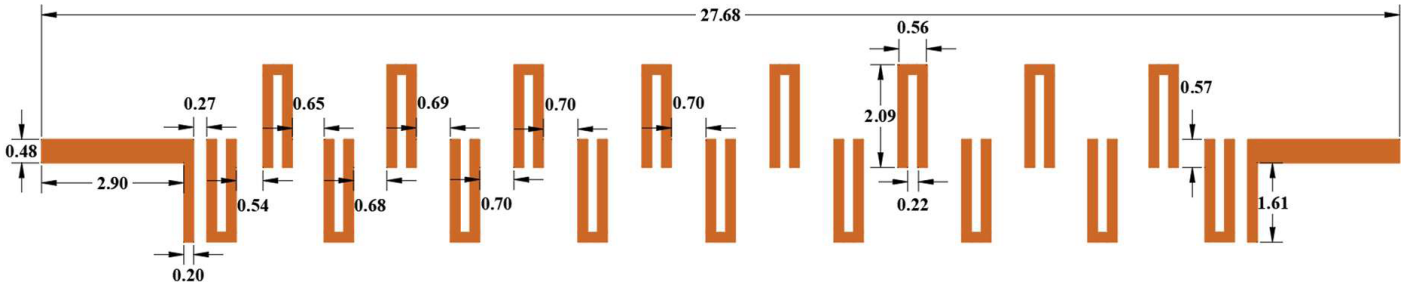

FIGURE 4. Schematic of the 17th-order hairpin filter.

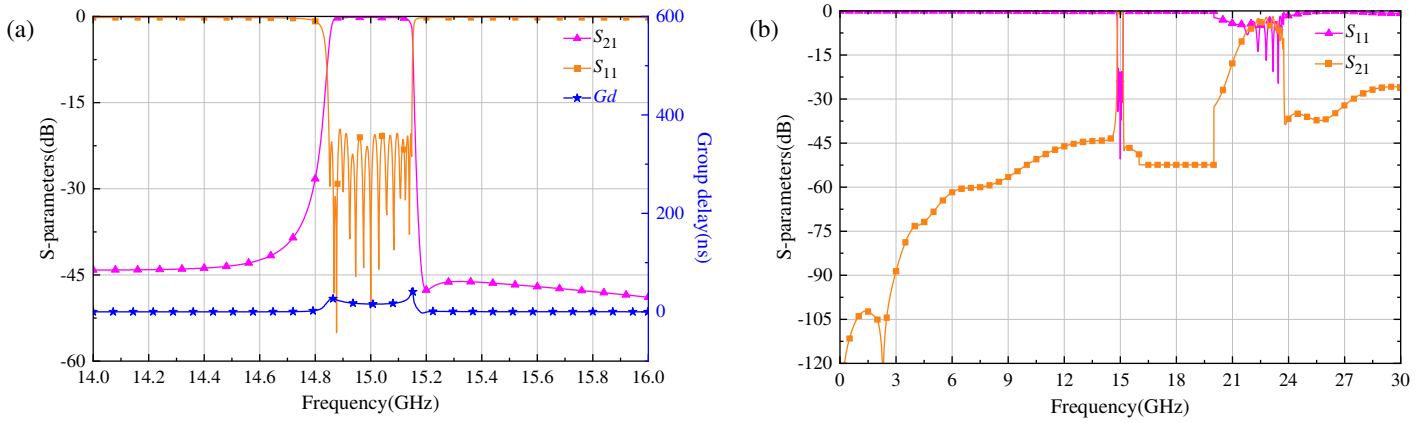

FIGURE 5. Filter simulation results. (a) A narrow perspective, (b) A wideband perspective.

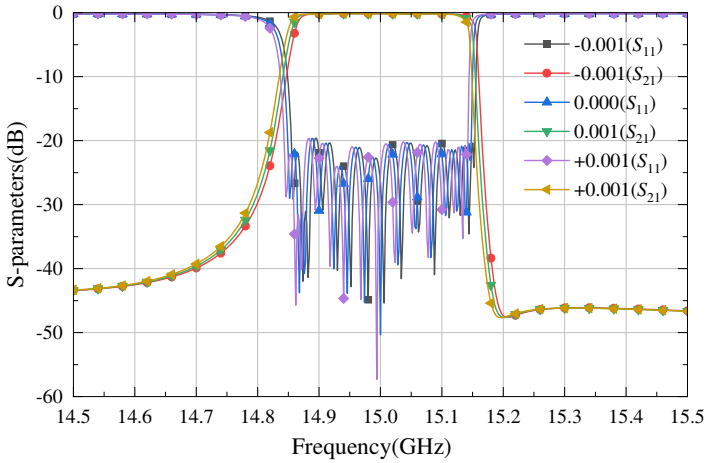

FIGURE 6. Sensitivity analysis.

gion. Fig. 5(b) The group delay variation within the 70% bandwidth is less than ± 7 ns. Overall, the simulated transmission characteristics were in good agreement with the theoretical design, providing a solid basis for subsequent device fabrication. Based on the accuracy of the adopted photolithography process, a fabrication tolerance sensitivity analysis has been carried out. The microstrip line width, which is one of the most critical geometrical parameters, is considered with a variation of $\pm 1\%$, corresponding to a dimensional deviation of ± 0.001 mm. The simulated results, as shown in Fig. 6, indicate that the filter response exhibits a certain frequency shift within the line width variation range of $+0.001$ mm to -0.001 mm. Nevertheless, these variations remain within an acceptable range for practical engineering applications, demonstrating that the proposed filter design possesses good robustness against fabrication tolerances.

At the operating frequency of 15 GHz, the surface current distribution of the proposed filter is analyzed. As shown in Fig. 7, the current is relatively uniformly distributed over the resonators without obvious current crowding. According to the analysis and experimental results reported in [27, 28], under similar operating conditions, the power-handling capability

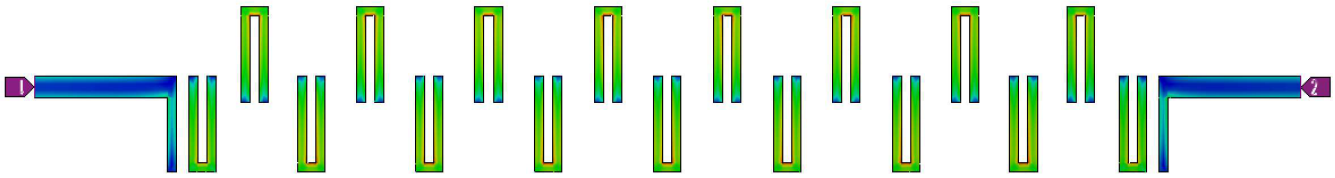

FIGURE 7. Surface current distribution at 15 GHz.

TABLE 2. Comparison with published bandpass filters.

Ref.	Order	f (GHz)	FBW (%)	IL (dB)	RL (dB)	Size (λg)	Filter Topology
[6]	3	15.12	3.48	1.38	10.1	69.1*42*10.7	groove-gap-waveguide
[9]	4	11	3	2.15	15	33.59*11.25	Substrate Integrated Waveguide
[11]	4	9.96	7.43	1.52	16.2	30.35*15.17	Substrate-Integrated Waveguide
[13]	4	12.46	3.67	1.36	15.28	27*27	Substrate Integrated Waveguide
[23]	5	14	5.71	0.7	14.5	16.65*15.15*77.8	Waveguide
[24]	4	15.13	3.44	0.76	9.6	160.91*91.5*14.7	Groove Gap Waveguide
[25]	3	10.18	3.2	2.33	16.13	25*25	Folded Substrate-Integrated Waveguide
[26]	N/A	14.39	5.56	1.6	15	6.81*14.38	substrate integration waveguide
This work	17	15	2	0.35	19.6	27.68*3.62	Microstrip

λ_g: the guided wavelength at the center frequency f_0.

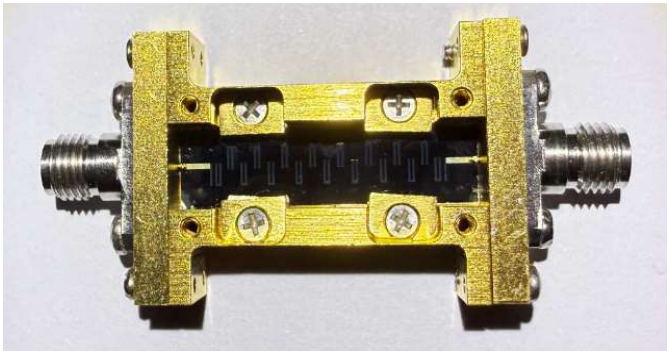

FIGURE 8. Photograph of the fabricated filter.

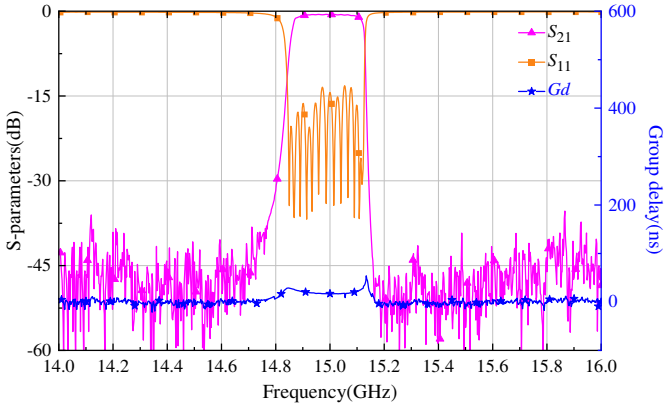

FIGURE 9. Measured results of the filter.

can exceed 20 dBm, which is sufficient for most practical high-temperature superconducting receiver front-end applications.

4. FABRICATION AND MEASUREMENT OF FILTER

In the fabrication process of the proposed design, high-precision photolithography was employed to deposit a $YBa_2Cu_3O_7$ high-temperature superconducting thin film on the surface of a high-permittivity thin substrate with a relative dielectric constant of 9.8, followed by accurate patterning to realize the designed hairpin resonator structures. The device layout and interconnections were implemented in accordance with the optimized coupling matrix parameters, ensuring precise spacing and coupling strength between the adjacent resonators. The fabricated filter has an overall physical size of 27.68 mm×3.62 mm×0.5 mm, as shown in Fig. 8.

The performance of the fabricated device was evaluated on a high-precision superconducting microwave measurement platform equipped with a liquid-nitrogen cryogenic temperature control system that stabilized the operating temperature at 77 K to fully exploit the low surface resistance characteristics of the HTS material. During the measurement, the S-parameters of the filter were characterized using a vector network analyzer. The measured responses showed excellent agreement with the IE3D simulation results, with the passband insertion loss, return loss, and out-of-band suppression meeting the design specifications, as illustrated in Fig. 9. These results not only validate the accuracy of the proposed design and fabrication processes but also demonstrate the high repeatability and engineering feasibility of the adopted fabrication technology and parameter optimization methodology for high-frequency HTS microstrip filters. Table 2 compares the performance parameters of the

filter proposed in this study with those of filters recently reported in the literature. The results indicate that, while maintaining favorable bandwidth characteristics, the proposed filter simultaneously achieves low insertion loss, compact size, and high return loss. In contrast, some existing designs exhibit difficulties in balancing bandwidth, loss, and overall size and commonly suffer from relatively large dimensions or higher insertion losses. Consequently, the proposed filter demonstrates promising application potential in terms of the overall performance.

5. CONCLUSION

The design of a seventeenth-order hairpin bandpass filter based on HTS thin-film technology operates at a center frequency of 15 GHz with a fractional bandwidth of 2%. The experimental results demonstrate a passband insertion loss below 0.35 dB, an *RL* better than 19.5 dB, and a stopband suppression exceeding 40 dB. The group delay variation within the 70% bandwidth is less than ± 8 ns. The good agreement between the simulation and measurement validates the effectiveness of the proposed design methodology and the fabrication process. By fully exploiting the low-loss characteristics of HTS materials and the compact coupling advantages of high-order hairpin resonators, the proposed structure achieves both a narrow bandwidth and high selectivity. The results indicate that the proposed design exhibits promising potential for high-performance Ku-band front-end filters and provides a valuable reference for future extensions to higher frequency bands and more complex systems.

REFERENCES

[1] Choi, J.-Y., J.-S. Ma, H. Oh, and W.-S. Kim, "A reconfigurable narrow-band bandpass filter using electrically-coupled open-loop resonators based on liquid crystals," *Journal of Physics D: Applied Physics*, Vol. 57, No. 46, 465307, 2024.

[2] Das, T. K. and S. Chatterjee, "Multi-spurious harmonics suppression in folded hairpin line bandpass filter by meander spurline," *International Journal of RF and Microwave Computer-Aided Engineering*, Vol. 31, No. 11, e22858, 2021.

[3] Feng, L.-Y. and H.-X. Zheng, "A miniaturized narrowband bandpass filter with wide stopband using open-loop resonator," *Microwave and Optical Technology Letters*, Vol. 53, No. 9, 2149–2152, 2011.

[4] Liu, H., S. Wang, J. Kuang, R. Wang, and H. Tian, "Compact HTS narrowband bandpass filter based on spiral D-CRLH resonator," *IEEE Transactions on Circuits and Systems II: Express Briefs*, Vol. 71, No. 3, 1007–1011, 2024.

[5] Jiang, X., Z. Xu, J. Xu, J. Guo, and C. Qian, "A miniaturized harmonic reject waveguide filter for ku-band VSAT transmitter," *IEEE Access*, Vol. 11, 46 164–46 172, 2023.

[6] Malki, M., L. Yang, and R. Gomez-Garcia, "Sharp-rejection inline groove-gap-waveguide bandpass filter with multiple transmission zeros for Ku-band application," *IEEE Microwave and Wireless Technology Letters*, Vol. 34, No. 5, 478–481, 2024.

[7] Morales-Hernández, A., M. A. Sánchez-Soriano, M. Ferrando-Rocher, S. Marini, and V. E. Boria, "In-depth study of the corona discharge breakdown thresholds in groove gap waveguides and enhancement strategies for inductive bandpass filters," *IEEE Access*, Vol. 10, 129 149–129 162, 2022.

[8] Sánchez-Soriano, M. A., S. Sirci, J. D. Martínez, and V. E. Boria, "Compact dual-mode substrate integrated waveguide coaxial cavity for bandpass filter design," *IEEE Microwave and Wireless Components Letters*, Vol. 26, No. 6, 386–388, 2016.

[9] Máximo-Gutiérrez, C., J. Hinojosa, and A. Álvarez melcon, "Narrowband and wideband bandpass filters based on empty substrate integrated waveguide loaded with dielectric elements," *IEEE Access*, Vol. 9, 32 094–32 105, 2021.

[10] Celis, S., M. Farhat, A. S. Almansouri, H. Bagci, and K. N. Salama, "Simplified modal-cancellation approach for substrate-integrated-waveguide narrow-band filter design," *Electronics*, Vol. 9, No. 6, 962, 2020.

[11] Jiao, M. R., F. Zhu, P. Chu, W. Yu, and G. Q. Luo, "Compact hybrid bandpass filters using substrate-integrated waveguide and stripline resonators," *IEEE Transactions on Microwave Theory and Techniques*, Vol. 72, No. 1, 391–400, 2024.

[12] Khan, A. A. and M. K. Mandal, "Narrowband substrate integrated waveguide bandpass filter with high selectivity," *IEEE Microwave and Wireless Components Letters*, Vol. 28, No. 5, 416–418, 2018.

[13] Liu, Q., D. Zhou, Y. Zhang, D. Zhang, and D. Lv, "Substrate integrated waveguide bandpass filters in box-like topology with bypass and direct couplings in diagonal cross-coupling path," *IEEE Transactions on Microwave Theory and Techniques*, Vol. 67, No. 3, 1014–1022, 2019.

[14] Liu, H., B. Ren, S. Hu, X. Guan, P. Wen, and J. Tang, "High-order dual-band superconducting bandpass filter with controllable bandwidths and multitransmission zeros," *IEEE Transactions on Microwave Theory and Techniques*, Vol. 65, No. 10, 3813–3823, 2017.

[15] Jin, S., B. Wei, B. Cao, X. Zhang, X. Guo, H. Peng, Y. Piao, and B. Gao, "Design and performance of an ultra-narrowband superconducting filter at UHF band," *IEEE Microwave and Wireless Components Letters*, Vol. 18, No. 6, 395–397, 2008.

[16] Yu, X., W. Xi, S. Wu, and P. Yan, "A 12-pole VHF band high selective high temperature superconducting filter," *Superconductor Science and Technology*, Vol. 34, No. 1, 015002, 2021.

[17] Li, C., X. Wang, J. Wang, L. Sun, and Y. He, "Progress on applications of high temperature superconducting microwave filters," *Superconductor Science and Technology*, Vol. 30, No. 7, 073001, 2017.

[18] Tao, L., B. Wei, X. Guo, B. Cao, and L. Jiang, "Miniaturized ultra-narrowband superconducting microstrip filter with stable coupling using optimized twin spiral-in-spiral-out resonators," *IEEE Transactions on Applied Superconductivity*, Vol. 29, No. 6, 1–7, 2019.

[19] Li, S., J. Huang, Q. Meng, L. Sun, Q. Zhang, F. Li, A. He, X. Zhang, C. Li, H. Li, and Y. He, "A 12-pole narrowband highly selective high-temperature superconducting filter for the application in the third-generation wireless communications," *IEEE Transactions on Microwave Theory and Techniques*, Vol. 55, No. 4, 754–759, 2007.

[20] Makimoto, M. and S. Yamashita, "Bandpass filters using parallel coupled stripline stepped impedance resonators," *IEEE Transactions on Microwave Theory and Techniques*, Vol. 28, No. 12, 1413–1417, 1980.

[21] Zhang, X., Q. Meng, F. Li, C. Li, S. Li, A. He, H. Li, and Y. He, "A 24-pole high T_c superconducting filter for mobile communication applications," *Superconductor Science and Technology*, Vol. 19, No. 5, S394–S397, 2006.

[22] Hong, J.-S. and M. J. Lancaster, "Couplings of microstrip square open-loop resonators for cross-coupled planar microwave fil-

ters," *IEEE Transactions on Microwave Theory and Techniques*, Vol. 44, No. 11, 2099–2109, 1996.

[23] Zhang, Y., X. Shang, F. Zhang, and J. Xu, "A 3-D printed Ku-band waveguide filter based on novel rotary coupling structure," *IEEE Microwave and Wireless Technology Letters*, Vol. 33, No. 1, 35–38, 2023.

[24] Malki, M., L. Yang, and R. Gómez-García, "Ku-band reflectionless single-and dual-band bandpass filters in groove gap waveguide," *IEEE Transactions on Microwave Theory and Techniques*, Vol. 73, No. 9, 5813–5827, 2025.

[25] Liu, Q., D.-W. Zhang, K. Gong, H. Qian, W.-Z. Qu, and N. An, "Single-and dual-band bandpass filters based on multiple-mode folded substrate-integrated waveguide cavities," *IEEE Transactions on Microwave Theory and Techniques*, Vol. 71, No. 12, 5335–5345, 2023.

[26] Yin, B., Q. Huang, H. Hao, and H. Zhang, "A high-selectivity double-mode SIW bandpass filter utilizing the modified parallel coupled microstrip lines," *Electromagnetics*, Vol. 41, No. 4, 263–274, 2021.

[27] Mansour, R. R., B. Jolley, S. Ye, F. S. Thomson, and V. Dokas, "On the power handling capability of high temperature superconductive filters," *IEEE Transactions on Microwave Theory and Techniques*, Vol. 44, No. 7, 1322–1338, 1996.

[28] Booth, J. C., D. A. Rudman, and R. H. Ono, "A self-attenuating superconducting transmission line for use as a microwave power limiter," *IEEE Transactions on Applied Superconductivity*, Vol. 13, No. 2, 305–310, 2003.